Geophysical Journal International

Geophys. J. Int. (2025) **241,** 941–953
Advance Access publication 2025 March 5
Geodynamics and tectonics

https://doi.org/10.1093/gji/ggaf084

Geodetic model of the 2024 January 22 M_w 7.0 Wushi (northwestern China) earthquake and M_w 5.7 aftershock from inversion of InSAR data

Nicola Angelo Famiglietti [1], Daniele Cheloni [2], Riccardo Caputo [3] and Annamaria Vicari[1]

[1] *Istituto Nazionale di Geofisica e Vulcanologia,* Sezione Irpinia, 83035 *Grottaminarda, Italy. E-mail: nicola.famiglietti@ingv.it*
[2] *Istituto Nazionale di Geofisica e Vulcanologia, Via di Vigna Murata* 605, 00143 *Roma, Italy. E-mail: daniele.cheloni@ingv.it*
[3] *Department of Physics and Earth Sciences, Ferrara University,* 44122 *Ferrara, Italy*

Accepted 2025 March 2. Received 2025 February 4; in original form 2024 July 22

SUMMARY

On 2024 January 22, an M_W 7.0 earthquake struck the southern sector of the Tian Shan Mountains in Wushi County, northwestern China, causing damage and casualties. In this study, using Interferometric Synthetic Aperture Radar measurements (Sentinel-1 satellites), we constrained the geometry of the fault segment responsible for the seismic event, the coseismic slip distribution, and the source of the subsequent M_W 5.7 aftershock deformation. Finally, we evaluated the potential state of stress of the unruptured portions of the causative fault as well as of adjacent fault segments, using the Coulomb stress failure function variations. Our findings indicate rupture along a transpressive left-lateral NNW dipping high-angle fault, associated with the Southern Tian Shan Fault alignment, likely the Maidan fault, with slip up to 3.5 m only occurring between 10 and 20 km depth. The position of the hypocentre with respect to our estimated slip distribution supports the evidence of a marked bilateral ENE–WSW rupture directivity during the mainshock. The modelling of the post-seismic deformation that includes the M_W 5.7 aftershock occurred on 2024 January 29, and that is located about 15 km to the south of the mainshock, indicates a main patch with up to 90 cm of slip that may have occurred on a shallow back-thrust segment, in agreement with the observed surface breaks. We propose a potential structural and/or lithological influence on the coseismic rupture extent, consistent with observations from other intracontinental earthquakes. Finally, based on the Coulomb stress distribution computation, we find that the M_W 5.7 aftershock was likely triggered by the preceding mainshock and that the Wushi earthquake also increased the stress level at both terminations of the modelled fault plane, particularly along the southwestwards continuation of the Maidan fault. In addition, we also find that a wide up-dip fault patch remained unruptured, and considering that these areas have been dynamically loaded it could represent potential further aseismic deformation and/or future significant ruptures, posing a continuing seismic hazard to Wushi County and surroundings areas.

Key words: Radar interferometry; Asia; Numerical modelling; Earthquake hazards; Earthquake source observations.

1. INTRODUCTION

The 2024 Wushi seismic sequence started on 2024 January 22 (18:09 UTC) with an M_W 7.0 event, followed by dozens of aftershocks, striking the southwestern sector of the Tian Shan Mountains in Wushi County (northwestern China) (Fig. 1), characterized by high geodetic strain rates (Wang & Shen 2020; Li *et al.* 2021). According to the United States Geological Survey (USGS), the earthquake's hypocentre was approximately 13 km deep, located in the Southern Tian Shan Mountains, about 130 km northwest of the city of Aykol. The earthquake was felt near the epicentre and across western Xinjiang Province, parts of eastern Almaty Region in Kazakhstan, and eastern Kyrgyzstan, resulting in damage and casualties. The subsequent seismic sequence included numerous aftershocks (eight events with magnitude between 5.0 and 5.7), located both ENE and WSW of the mainshock (USGS

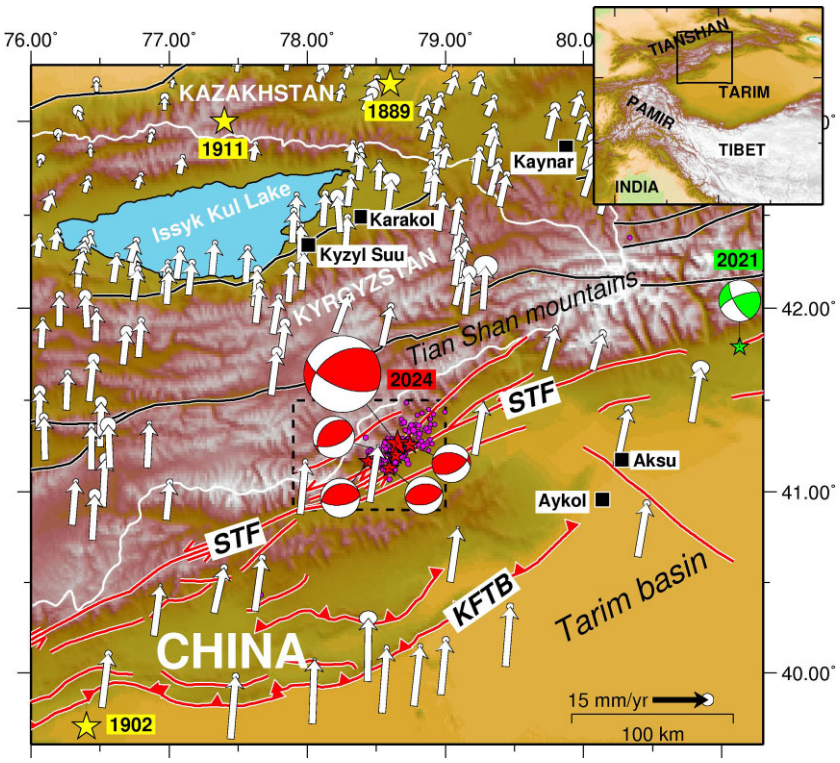

Figure 1. Seismotectonic framework. Solid barbed lines denote major tectonic lineaments (Wu *et al.* 2024). Seismicity: dots indicate all instrumental earthquakes occurring between January 22 and February 26 without any selection based on magnitude or depth from the United States Geological Survey catalogue (USGS 2024); red stars represent significant shocks ($M > 5$), including the 2024 January 22, M_W 7.0 mainshock; the green star marks the 2021 M_W 5.3 Baicheng transpressive earthquake, occurring NE of the 2024 seismic sequence on a high-angle fault segment along the front of the southern Tian Shan mountains (Yushan *et al.* 2022); the yellow stars are large ($M > 7$) historical events. Arrows show the GPS velocity field in a Eurasian reference frame, illustrating the relative motion of the Tarim basin compared to the Kazakh platform (Wang & Shen 2020). The upper inset presents a tectonic sketch of western China, with the box indicating the area of the main figure. The dashed box indicates the area of Figs 2 and 3 (upper panels). Abbreviations: KFTB = Kepingtage Fold-and Thrust Belt; STF = Southern Tianshan Fault.

database). The focal mechanism solution for the main events indicate transpressional faulting with reverse dip-slip and left-lateral kinematic components (USGS 2024), in agreement with the direction of active shortening of about 10 mm yr^{-1} in this sector of the Tian Shan Mountains (Molnar & Ghose 2000; Wang & Shen 2020). In addition, a recent study (Zhang *et al.* 2024) has highlighted a zone of surface ruptures (extending for about 2 km), possibly associated with a SE-dipping fault (thus dipping in the opposite direction compared to the mainshock fault plane) that might be related to the M_W 5.7 largest aftershock occurred on 29 January.

The Tian Shan Mountains are a convergent orogenic belt within the Eurasia continent, reactivated in response to the India–Eurasia collision (e.g. Avouac *et al.* 1993), and characterized by an intense present-day tectonic deformation. The epicentral area is marked by the presence of several ENE–WSW trending reverse and left-lateral strike-slip fault systems parallel to the range (e.g. Thompson *et al.* 2002), in both the piedmont region and the interior of the mountain (Fig. 1). In particular, foreland thrust faults and folds, such as the Kepingtage Fold-and-Thrust Belt (KFTB), accommodate most of the crustal shortening on the southern side of the Tian Shan orogen (e.g. Avouac *et al.* 1993; Shen *et al.* 2001; Huang *et al.* 2015), while the faults located in the interior mountain range are characterized by a component of strike-slip motion, like the Southern Tianshan Fault (STF) which includes in the epicentral area the Maidan fault segment. The latter is a sinistral reverse fault extending for more than 400 km, and representing at depth the crustal boundary between the Tarim Basin and the southwestern Tian Shan. The contemporaneous activity of KFTB and STF are a consequence of the slip partitioning due to the oblique Indo-Eurasian convergence and reactivation of inherited structures within the Tian Shan crustal block.

In this study we present a comprehensive data set of Interferometric Synthetic Aperture Radar (InSAR) measurements (Sentinel-1 satellites), including five interferograms covering the earthquake and parts of the post-seismic period and provide a combined analysis of the 2024 Wushi seismic sequence. In particular, using elastic dislocation models, we estimate the geometry and the distribution of slip during the main seismic event, and investigate the source of the subsequent aftershock deformation. We incorporate information on aftershock distribution and on known geological structures of the area for validation. Additionally, we examine static Coulomb stress changes induced by the mainshock, assessing their contribution to aftershock triggering during the 2024 Wushi sequence and to the possible loading of the unruptured portions of the coseismic fault plane as well as of adjacent fault segments.

2. TECTONIC SETTINGS AND SEISMICITY

Wushi County in Xinjiang (northwestern China) sits at the central southern sector of the Tian Shan mountain chain along the Tuoshigan valley (Fig. 1). Although the India–Eurasia plate boundary is

more than 1000 km away, the local stress field is strongly influenced by the Himalayan collision. The combination of the induced stresses with the existence of a Palaeozoic suture zone (e.g. Yin 2010) caused a strong deformation and the rapid uplift of the Tianshan Range since ca. 26 Myr (Li *et al.* 2013). The progressive convergence of the relatively rigid continental blocks of the Tarim Basin, to the south, and the Kazakh Platform and Junggar Basin, to the north, generated a double vergence orogen associated with the reactivation of many inherited structures. Along the southern side, the convergence rate is still approximately 10 mm yr^{-1} (Wang & Shen 2020). As a consequence, the Tian Shan Mountains form a seismically active intracontinental mountain belt, stretching approximately 2500 km in an ENE–WSW direction north of the Tarim Basin (Fig. 1). Due to the oblique orientation of the stress trajectories relative to the range, a diffuse slip partitioning developed within the crustal volume undergoing deformation as it is clearly documented by the contemporaneous activity of both low-angle thrust fault systems in the piedmont region (Zubovich *et al.* 2010) and high-angle sinistral reverse faults in the mountain interior (Shen *et al.* 2001; Wu *et al.* 2019; Qiu *et al.* 2022).

Seismic activity in the southwestern Tian Shan primarily stems from large ($M > 7$) historical and paleo- earthquakes generated by low-angle foreland folds and thrust faults, situated approximately 80–100 km south of the high-angle STF. Notably, three significant events occurred in the western Tian Shan region (Fig. 1): the 1889 M8.3 Chilik thrust event in the northern piedmont (Krüger *et al.* 2015), the 1902 M_S 8.3 Artux earthquake located within the accretionary wedge in the southwestern piedmont (Kulikova & Krüger 2017), and the 1911 M_S 8.2 Kemin oblique slip event in the northern Tian Shan (Kulikova & Krüger 2015).

On the contrary, in the epicentral area of the 2024 earthquake, events with a magnitude of 7 or greater are likely infrequent, lacking any historical record associated with the Maidan fault segment of the STF, where only few earthquakes of magnitude $M > 6$ were recorded. In a recent geological study, Wu *et al.* (2020) suggest however that the Maidan fault is still active and indeed generated large earthquakes during the Holocene, therefore being associated with a high seismic hazard. Accordingly, the 2024 January 22, M_W 7.0 earthquake represents the most powerful instrumentally recorded event along the high-angle Southern Tian Shan Fault in northwestern China. Actual Global Navigation Satellite Systems (GNSS) data confirm that deformation across the southern Tian Shan is still active, accommodating about 4.0 mm yr^{-1} NNW–SSE oriented crustal shortening between the foreland and the Kepintage thrust belt, and about 2.2 mm yr^{-1} of crustal shortening across the high-angle STF (Zubovich *et al.* 2010).

3. SENTINEL-1 SAR DATA

We used SAR data acquired by the Sentinel-1 (C-band) satellites from the European Space Agency in Terrain Observation by Progressive Scans mode, to analyse the coseismic displacement field caused by the 2024 January 22, M_W 7.0, earthquake. Specifically, we utilized two interferometric pairs (ascending and descending) from tracks A056 and D034 to measure the coseismic displacement (T1) (Fig. 2 upper panels; and Fig. S1 middle panels, Table S1, Supporting Information), and an additional descending interferogram from track D136 to capture cumulative ground displacement (T1 + T2) resulting from the mainshock and the subsequent post-seismic phase (Fig. S1, upper panels; Table S1, Supporting Information), including the M_W 5.7 aftershock occurred on 2024 January 29. We also examined two other interferograms (from tracks A056 and D034) to study aftershock deformation (T2) triggered by the mainshock (Fig 2; and Fig. S1 bottom panels, Table S1, Supporting Information). This data, with different incidence angles and temporal frames, enabled us to comprehensively analyse both the M_W 7.0 earthquake and M_W 5.7 aftershock displacement fields, as well as generate a cumulative deformation map (Figs S2, S3 and S4, Supporting Information), hence to better constrain the source modelling of the causative faults as well.

All interferograms were processed using classical two-steps SAR interferometry (e.g. Famiglietti *et al.* 2022) implemented in the SARscape® software, part of the ENVI package. A Digital Elevation Model (DEM) with 30 m spatial resolution from the ALOS World 3D catalogue was employed to account for topography during processing (Takaku *et al.* 2014). To enhance SAR image quality and reduce speckle noise, a 4 × 1 multilook factor was applied to Sentinel-1 data, resulting in a final pixel dimension of 15 m on the ground. Interferograms were filtered using the Goldstein method (Goldstein *et al.* 1998) to enhance signal-to-noise ratio. In particular, the adaptive filtering approach used, an extension of the Goldstein method, significantly improved fringe visibility and reduced noise introduced by temporal or baseline-related decorrelation. In this configuration, the 'alpha' parameter depends on the coherence: incoherent areas were filtered more than coherent zones. This minimized signal loss while strongly reducing noise levels. To optimize its performance, the 'alpha' parameter, which determines the filter's strength, is adaptively adjusted based on the local scene coherence (Ghulam *et al.* 2010). Then, phase unwrapping was performed using the Delaunay Minimum Cost Flow algorithm (Costantini 1998), followed by geocoding of the unwrapped phase using the DEM in the UTM WGS84 reference system. This method is similar to the traditional Minimum Cost Flow method, with the primary difference being that the grid does not necessarily cover all image pixels, but only those above the 'Unwrapping Coherence Threshold' (in this study = 0.3). Additionally, it uses a Delaunay triangular grid instead of a square one. As a result, only points with good coherence are unwrapped, without any influence from low-coherence pixels. The utilization of Delaunay triangulation is especially advantageous when multiple low-coherence areas are scattered throughout the image; in such cases, other unwrapping approaches might produce phase jumps, whereas the Delaunay approach minimizes these jumps (Reigber & Moreira 1997).

The unwrapped coseismic (T1) and the cumulated (T1 + T2) interferograms reveal ground displacement toward the satellite, concentrated in the hanging wall of the mainshock with an ENE–WSW striking deformation lobe along the STF (Fig 3; Figs S2, S3 and S4, Supporting Information). Displacement in E–W and vertical directions was also estimated from ascending and descending interferograms (Fig. S5, Supporting Information). Uplift across the oblique thrust fault is significant (Fig. S5, left panels, Supporting Information), with a maximum LOS (Line-of-Sight) displacement of about 70 cm SW of the epicentre. The observed deformation suggests a blind rupture consistent with one of the mainshock's focal mechanisms, possibly indicating rupture along a steep NNW-dipping fault, and thus consistent with the transpressional mechanisms of the STF.

Post-seismic interferograms (Fig 4; Figs S2 and S3, Supporting Information), covering about 1 month of post-seismic deformation following the mainshock and including the M_W 5.7 aftershock on 2024 January 29, show a small lobe of LOS displacements toward the satellite, with a maximum LOS of more than 20 cm. The clear LOS deformation gradient observed particularly in the

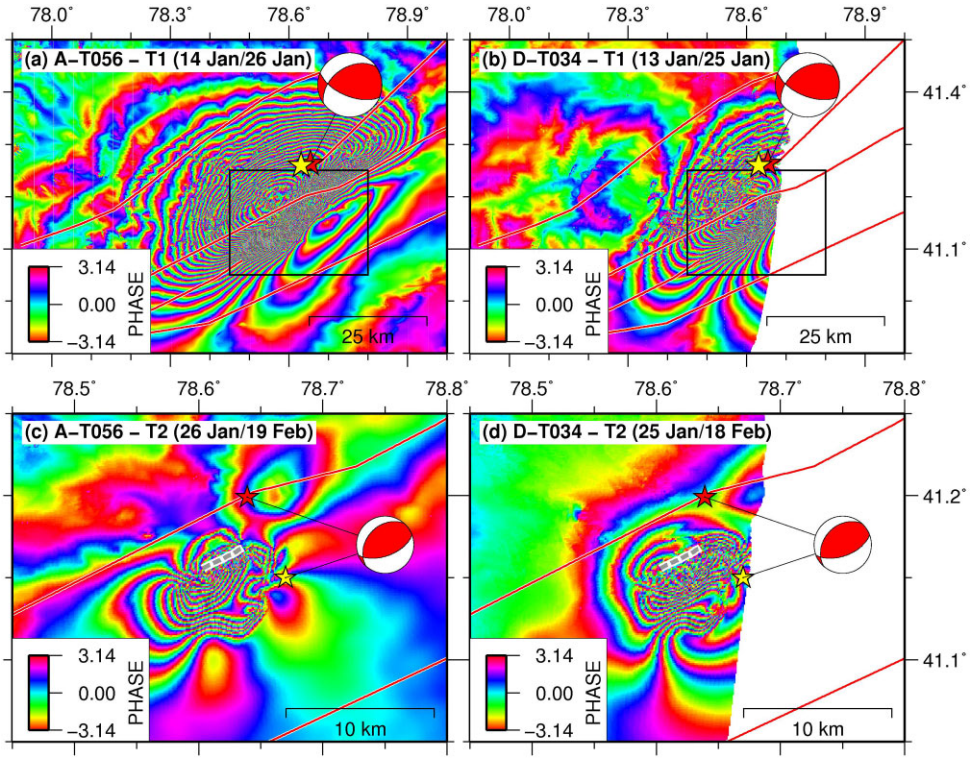

Figure 2. Sentinel-1 wrapped interferograms of the 2024 January 22, M_W 7.0, Wushi mainshock and the 2024 January 29, M_W 5.7 aftershock. The red and yellow stars are the mainshock provided by USGS and Liang *et al.* (2024), respectively, with its focal mechanism. In the bottom panels, the smaller red and yellow star represents the M_W 5.7 aftershock that occurred on January 29 provided by USGS and Liang *et al.* (2024), respectively, with its focal mechanism. Solid lines are the major faults of the area (Wu *et al.* 2024). The black box in the upper panels indicates the area of the bottom panels. The grey dashed line in the post-seismic (T2) interferograms indicates the location of the observed surface ruptures (Zhang *et al.* 2024).

ascending interferogram (Fig. S2, Supporting Information) and the orientation of this deformation lobe, well coincide with the trace of the observed surface ruptures (Zhang *et al.* 2024). The distinct spatial positions of mainshock and aftershock displacement patterns suggest therefore different slip locations associated with the mainshock and aftershock along the same rupture fault, or the activation of a different and shallower structure during the M_W 5.7 aftershock. Finally, the cumulated descending interferogram (T1 + T2) illustrates the combined effects of the mainshock and subsequent aftershock deformation (Fig. 3, bottom panels, and Fig. S1,upper panels, Supporting Information).

4. GEODETIC MODELLING

We performed the source modelling using rectangular dislocations embedded in an elastic, homogeneous and isotropic half-space (Okada 1985), to image the fault geometry and slip distribution of the 2024 January 22, M_W 7.0 Wushi earthquake and the source of the following deformation associated with the M_W 5.7 aftershock, using a standard two-steps procedure (e.g. Atzori *et al.* 2009; Cheloni *et al.* 2010, 2024; Golshadi *et al.* 2023): (1) We inverted the LOS displacements to retrieve the fault geometry, and then (2) the best-fit uniform slip fault solution is used as *a-priori* for the estimation of the coseismic slip distribution. Before modelling, the InSAR displacement maps were down-sampled using a resolution-based down-sampling scheme (Lohman & Simons 2005).

In the first step, we carried out a nonlinear optimization of the fault geometry responsible for the mainshock by using a simulated annealing algorithm (Corana *et al.* 1987). Then, to estimate the confidence intervals of the retrieved model parameters we used a Monte Carlo simulation technique (Press *et al.* 1992) which applies the best-fitting technique to a large number of synthetic data sets (500), each one derived from adding synthetic realizations of data noise to the actual data set. The individual model parameters appear to be well resolved with compact formal 95 per cent confidence intervals; however, despite this formal resolution, there are trade-offs between the model parameters, which may lead to an underestimation of the standard deviations (Fig. S6, Supporting Information and Table 1). Moreover, real geological complexities may introduce additional uncertainties that go beyond those accounted for in our formal calculations. Features such as non-planar faults and crustal heterogeneity are indeed difficult to quantify precisely and could significantly contribute to larger uncertainties. The best-fitting uniform slip solution of the 2024 January 22, M_W 7.0 Wushi earthquake is described by a 230° striking and 62° NW dipping oblique thrust (rake about 47°) 36 km × 12 km fault plane passing through the hypocentral location (Fig. 5, black box) and in good agreement with the steeply dipping plane of the seismological focal solution (strike/dip/rake 235°/45°/42°) (USGS 2024). The average uniform slip is 2.7 m, which assuming a value of 30 GPa for rigidity, yields an estimated seismic moment of 3.61×10^{19} Nm, equivalent to a M_W 7.0 earthquake.

In the second step, to estimate a more realistic coseismic slip distribution on the fault plane, we extend the uniform slip fault in order to capture the area affected by aftershocks (60 km × 30 km) and subdivide the fault into small patches of variable size, with increasing patch size with depth to maintain a good model resolution at the deeper portions of the fault (Cheloni *et al.* 2016). The

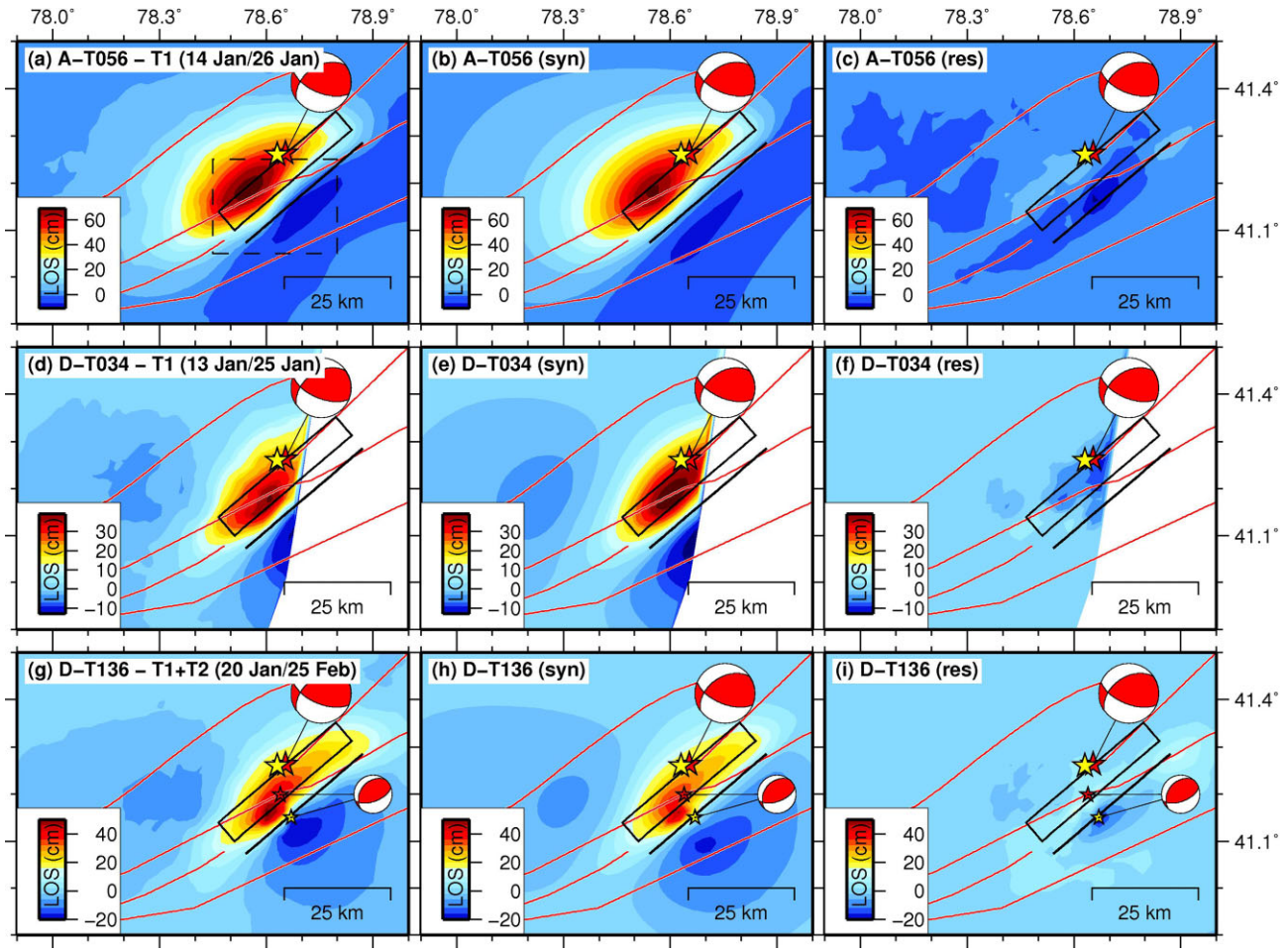

Figure 3. Displacement maps of the 2024 January 22, M_W 7.0, Wushi earthquake sequence. Observed (left panels), modelled (middle panels) and residuals (right panels) InSAR Sentinel-1 ascending and descending unwrapped interferograms based on our best-fit model. The black box represents the best-fit uniform slip solution. The red and yellow stars are the mainshock provided by USGS and Liang *et al.* (2024), respectively, with its focal mechanism. In the bottom panels, the smaller red and yellow star represents the M_W 5.7 aftershock that occurred on January 29 provided by USGS and Liang *et al.* (2024), respectively, with its focal mechanism. The dashed box in panel (a) indicates the area of Fig. 4. Other symbols as in Fig. 2.

shallower patches are 1.25 km × 1.25 km, while the deeper ones are approximately 4.3 km × 4.3 km. Additional terms consisting of a linear ramp for each InSAR displacement map are also included in the inversion to minimize the effect on the solution of any residual long-wavelength orbital signal in InSAR images. We also apply positivity constraints (Stark & Parker 1995) and regularize the linear inversion by applying spatial smoothing (using the Laplacian operator), choosing the optimal smoothing weight factor by examining a trade-off curve of weighted misfit versus model roughness (Fig. S7, Supporting Information).

To further evaluate the consistency of the model and to provide a benchmark for comparison, we calculated the theoretical displacements at the three nearest GNSS stations using the best-fitting coseismic slip distribution. This calculation was also aimed at encouraging the owners of raw GNSS data or derived displacement vectors to make these observations available, either to confirm the prediction or, implausibly, to claim to invalidate it. The results (Fig. 5, white arrows) show that the predicted displacements are in the order of a few centimeters for the closest station, and they decrease rapidly with distance.

To qualitatively assess the model resolution, we performed a set of synthetic tests (Figs S8 and S9, Supporting Information) in which we imposed slip at different depths and particular configurations of slip on the fault plane (i.e. checkerboard tests). The input slip models were then used to generate synthetic InSAR displacements. The inversion of synthetic surface displacements produced with the different input slip models show that long wavelength slip features are well resolved at each depth range (Fig. S8, Supporting Information), and that our InSAR data set is able to discriminate between shallow and deep portions of the fault that may have slipped coseismically. The checkerboard tests show that 10 km wavelength features are well resolved in the upper and central portions of the fault plane, whereas input slip features appear significantly smeared at down-dip depth > 20 km (Fig. S8, Supporting Information).

4.1. Different hypotheses on the geometry of the source of the M_W 5.7 aftershock deformation

As we state in paragraph 2, the distinct spatial positions of coseismic and post-seismic displacement patterns (Figs 2, 3 and 4) suggest different depths and locations of coseismic and aftershock slip. The observed post-seismic displacement could have happened either on the shallower portions of the same coseismic rupture plane, or on a different structure, as for example a shallower splay.

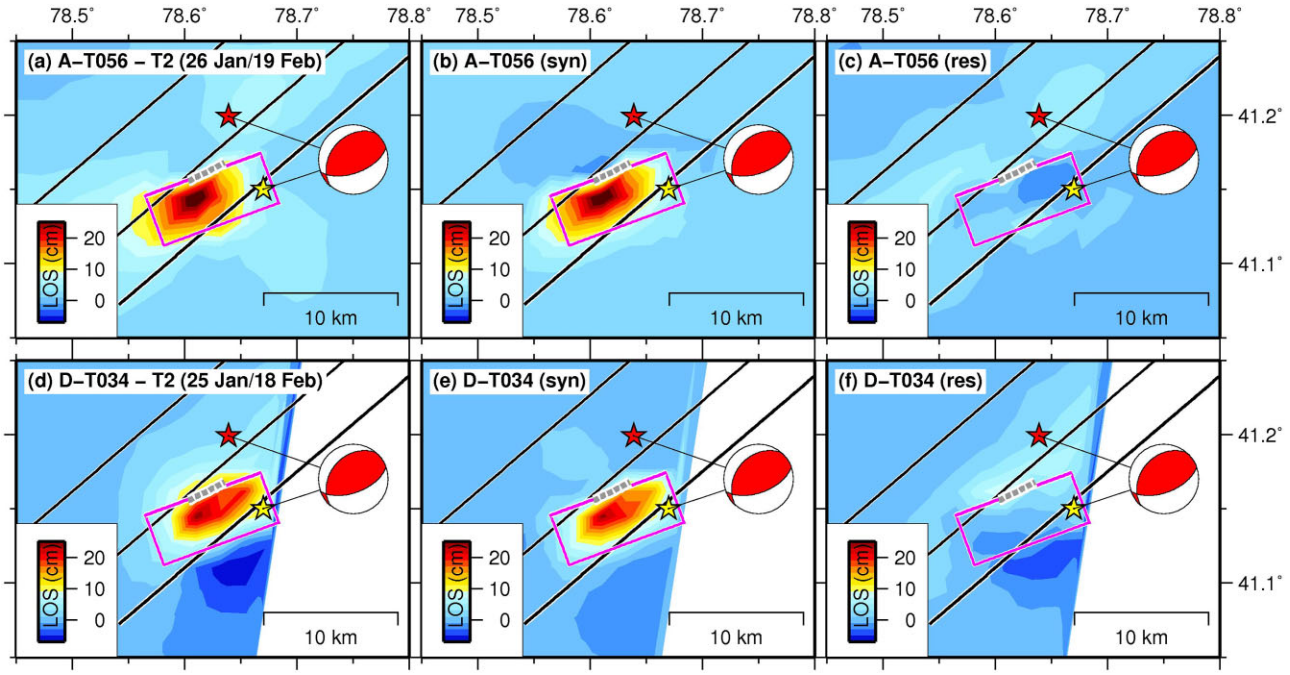

Figure 4. Displacement maps of the 2024 January 29, M_W 5.7 aftershock. Observed (left panels), modelled (middle panels), and residuals (right panels) InSAR Sentinel-1 ascending and descending unwrapped interferograms based on our best-fit model. The black and violet boxes represent our best-fit uniform slip solutions for the mainshock and aftershock, respectively. The grey dashed line indicates the observed surface ruptures (Zhang *et al.* 2024). The red and yellow stars are the M_W 7.0 mainshock and the M_W 5.7 aftershock provided by USGS and Liang *et al.* (2024), respectively, with their focal mechanism. Other symbols as in Fig. 2.

Moreover, as already noticed in Yu *et al.* (2024), the post-seismic NE-trending deformation lobe that includes the M_W 5.7 aftershock (T2), is consistent with the displacement of the surface rupture that was recently identified by Zhang *et al.* (2024) from a field geological expedition. This surface rupture zone has a general trend of N60°E and extends for about 2 km, just in the correspondence of the observed maximum post-seismic deformation gradient (Figs 2, 4, 6; and Fig. S2, Supporting Information). According to the authors, the characteristics of this rupture zone (displaying a maximum vertical offset of about 1 m) are mainly controlled by a SE-dipping reverse fault, that is, opposite in dip direction to the causative fault of the mainshock. Although, the authors (Yu *et al.* 2024; Zhang *et al.* 2024) speculated that the seismogenic fault of the aftershock (and of the associated surface deformation) was this thrust fault, they never actually fully explored this possibility and the InSAR post-seismic data have never been inverted to test this hypothesis.

For this reason, in this section, we explore different possible geometries of the fault segment responsible for the observed post-seismic deformation, that includes the M_W 5.7 aftershock. To this end we performed a number of joint inversions varying the geometry and the position of the possible source of the post-seismic deformation to investigate how this might affect our results. In particular, we explored three different hypotheses, assuming additional slip occurring on the major coseismic fault, on a synthetic thrust (NW-dipping) and on a back-thrust (SE-dipping), respectively.

Both the results of the first and second models (Fig. 6) show a main patch of slip located up-dip with respect to the mainshock hypocenter, with maximum slip of about 100 cm, equivalent to a moment magnitude of about M_W 5.9. In the first model, the slip occurred on coplanar patch of the coseismic causative fault (Fig. 6a), whereas the second model implies that slip occurred on a synthetic thrust (strike/dip/rake 238°/55°/93°) (Fig. 6b), but very close to the main fault plane. The last model is assuming further slip on an SE-dipping fault (i.e. a back-thrust) (Fig. 6c), fixing its position based on the surface ruptures observed in the field. Also in this case, the model shows a main patch of slip shallower than the hypocentre mainshock, with maximum slip of about 90 cm, potentially reaching the surface just in correspondence of the observed surface breaks (Fig. 6c). Since the RMS of the data is similar in all three cases (Table S3, Supporting Information), but the last model also aligns with the field observations, we therefore favour the assumption that this slip occurred on a fault antithetic to the mainshock rupture plane. Another possibility is that both the SE-dipping fault and the synthetic fault moved. By inverting the data for three faults (the main one and the two secondary ones during the post-seismic deformation), the misfit on the data does not improve compared to the two-fault model, with the maximum slip concentrating on the SE-dipping secondary fault. Thus, we adopt as our final model a main fault plane composed by an NW-dipping steep fault, and by only a secondary fault dipping in the opposite direction (i.e. SE-dipping).

4.2. Coseismic slip on the STF oblique thrust and aftershock slip on a shallow back-thrust

The results of the joint inversion for mainshock and aftershock slip distributions on the main oblique thrust fault and on the minor back-thrust are shown in Figs 5, 6 and 7. The inversion of the displacement maps of the two deformation frames (T1 and T2) satisfactorily reproduces the observed InSAR displacements (Figs 3 and 4; RMS values in Table S2 in the Supporting Information). In our model, the January 22 mainshock (T1) occurred on a segment of the STF, releasing a seismic moment of 3.96×10^{19} Nm (using a value of 30 GPa for rigidity), equivalent to an M_W 7.03 earthquake

Table 1. Source parameters of the 2024 January 22, M_W 7.0 Wushi earthquake.

Model	Lon (°)	Lat (°)	Depth (km)	Length (km)	Width (km)	Strike (°)	Dip (°)	Slip (m)	Rake (°)	Mw
F1 uniform	78.67* (−0.27; 0.24)	41.21* (−0.11; 0.37)	7.4 (−0.5; 0.6)	36.3 (−0.9; 0.9)	12.1 (−1.2; 1.7)	229.7 (−0.9; 0.4)	61.6 (−1.4; 0.5)	2.72 (−0.32; 0.27)	47.2 (−1.9; 0.5)	7.01
F2 variable	"	"	0.0	60.0	30.0	"	"	"	"	7.02
InSAR N2024	78.64	41.23	6.6	34.7	10.5	230.3	57.5		41.7	7.10
InSAR G2024				60.0	30.0	235.0	55.0			7.0
InSAR Y2024				90.0	30.0	229.0	62.8	4.0	49.8	7.02
USGS	78.65	41.27	13.0			235.0	45.0		42.0	7.0

Values in parenthesis represent the individual formal 95 percent confidence intervals determined using a Monte Carlo method.
Abbreviations: (*) middle point along the upper edge of the fault (uncertainties in km); N2024, Nai *et al.* (2025); G2024, Guo *et al.* (2024); Y2024, Yu *et al.* (2024).

Figure 5. Geodetic model of the 2024 January 22, M_W 7.0 Wushi earthquake. Panel (a) depicts fault geometry and coseismic slip distribution of the mainshock. Solid lines represent major faults (Wu *et al.* 2023). Seismicity is indicated by magenta circles (aftershocks between January 22 and February 26 from USGS catalogue) and yellow circles ($M > 4$ events from Liang *et al.* 2024), with stars denoting the largest events of the seismic sequence (red stars from USGS, yellow from Liang *et al.* 2024). Beach-balls display mainshock and greatest aftershock focal solutions from USGS catalogue. The black box represents the best-fit uniform slip solution. The blue line represents the Tuoshigan River. Arrows show the expected coseismic displacements at the nearest GPS stations, as computed by our geodetic model. The dashed box indicates the area of Fig. 6. The inset (b) shows a cross-section perpendicular to the fault strike, displaying slip distribution at depth. Note: many hypocentres were fixed at 10 km depth from USGS location.

(Table S3, Supporting Information). The slip pattern is similar to that found in the preliminary finite-fault model as provided by the USGS (USGS 2024), showing a main coseismic asperity (up to 3.5 m of slip) occurred in horizontally elongated patches roughly located across the centre of the plane, up-dip and WSW and ENE with respect to the mainshock hypocentre, thus implying a bilateral directivity for the Wushi mainshock which left unbroken the upper part of the reactivated tectonic structure.

For the deformation associated with the M_W 5.7 aftershock (T2), our preferred model assumes slip on a secondary back-thrust fault (strike/dip/rake 70°/41°/90°) whose surface trace has been constrained by the observed surface ruptures (Zhang *et al.* 2024), which released a total seismic moment of 0.07×10^{19} Nm, equivalent to a M_W 5.85 earthquake (Table S3, Supporting Information). Estimated aftershock slip occurred on one main patch reaching the topographic surface with a maximum slip of 90 cm occurring at a depth of ∼1.5–2.0 km, with the maximum slip located just beneath the observed surface ruptures (Fig. 6c).

5. STATIC COULOMB STRESS CHANGE

It is now well established that coseismic slip after a major earthquake can lead to changes in static stress, potentially triggering further earthquakes and aseismic slip episodes on nearby faults or unbroken segments of the causative fault itself (e.g. Lin & Stein 2004; Lin *et al.* 2011; Cheloni *et al.* 2016). In this context, to assess hazard in the study area and to investigate the potential triggering relationships between the mainshock and the greatest aftershock, it is crucial to

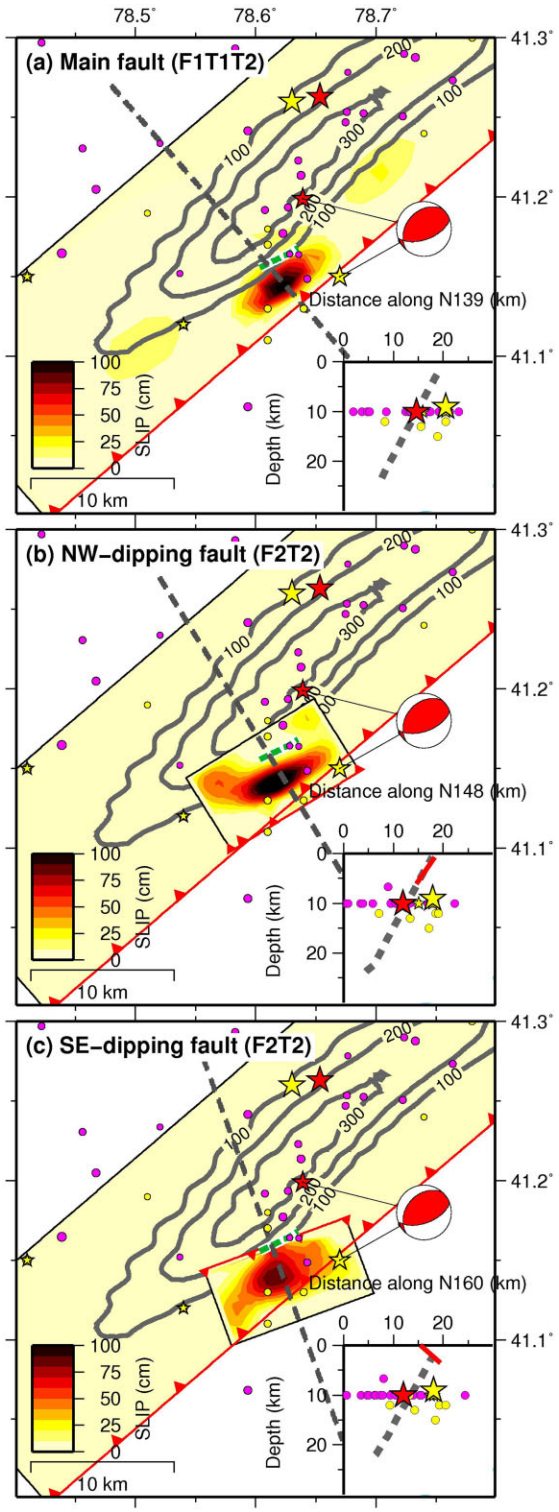

Figure 6. Geodetic models of the post-seismic deformation including the 2024 January 29, M_W 5.7. (a) Assuming that slip occurred on the same coseismic plane, (b) on an NW-dipping splay and (c) assuming slip on a SE-dipping fault. The estimated fault plane (yellow box) and coseismic slip of the 2024 January 22, M_W 7.0 Wushi mainshock is shown for comparison (contours in cm, in grey). The green dashed line indicates the observed surface ruptures (Zhang *et al.* 2024). The insets show the different fault models (red lines) as a function of depth for the different assumed activated thrust segments. Also shown is the position of the coseismic fault plane (dashed grey line). Other symbols as in Fig. 5.

evaluate: (1) the stress state of unruptured parts of the main causative fault, (2) the state of stress of the secondary fault induced by the mainshock, and (3) which other faults in the southwestern Tian Shan region might be brought closer to failure by stress changes from the 2024 earthquake.

In the both case, we calculated the Coulomb stress change induced by the mainshock using our preferred slip distribution (Figs 5 and 7) assuming an effective friction coefficient of 0.4, as is commonly used in stress interaction studies (e.g. Freed 2005; Akinci & Antonioli 2013). As expected, on the main fault we find increased stresses in the upper and lower parts of the fault plane surrounding the coseismic rupture area (Fig. 7b). On the secondary SE-dipping fault the shape of the slipped area corresponds well with the pattern of increased stresses (Fig. 7d), suggesting that the aftershock deformation event was possibly triggered by the preceding January 22 M_W 7.0 earthquake.

Finally, we computed Coulomb stress changes from our preferred slip distribution on (a) NW-dipping fault segments with the same mechanism of the largest aftershocks [i.e. with a more reverse rake angle (Liang *et al.* 2024)], and (b) on SE-dipping thrusts. We observed increased Coulomb stress at both terminations of the modelled fault plane at hypocentral depths (Fig. 8a), particularly along the southwestwards continuation of the Maidan fault. Additionally, increased stress was found on the Toxkan fault located north of the Maidan fault (Fig. 8). On the southern Wensubei reverse fault, decreased stress was noted especially southwards of the epicentral area. Examining cross-section A–A′ in Figs 8(a) and (b), it is evident that a blind coseismic rupture increases the stress over much of the upper crust, especially along its up-dip continuation for both NW-dipping and SE-dipping reverse faults. These near-surface regions of stress increases are sometimes relieved by secondary surface faults (Lin & Stein 2004). In fact, secondary surface faulting was observed following the 2024 M_W 7.0 Wushi earthquake (Zhang *et al.* 2024), exactly in a region of increased Coulomb stress (Fig. 8), where our secondary SE-dipping fault is located (see green line in section A–A′ of Fig. 8b).

6. DISCUSSIONS AND CONCLUSIONS

The 2024 January 22, M_W 7.0 Wushi earthquake in northwestern China represents the largest seismic event recorded with modern geodetic measurements in the southern Tian Shan Mountains. We performed joint inversions of a comprehensive geodetic data set for distributed slip during the January 22 mainshock and the following M_W 5.7 aftershock occurred on 2024 January 29, to determine which segment of the Southern Tian Shan Fault was activated by the 2024 mainshock, and the source of the aftershock deformation.

The dislocation modelling of InSAR data has revealed that the January 22 M_W 7.0 mainshock was caused by the rupture of a ∼60° NNW-dipping, ∼36 km-long oblique-slip fault, which exhibits both reverse and left-lateral movements (rake ∼47°), with a major slipping patch in the middle of the plane, in good agreement with previous inversions of geodetic data (Guo *et al.* 2024; Nai *et al.* 2025; Yu *et al.* 2024) and moment tensor solutions (Liang *et al.* 2024; USGS 2024). According to the different authors and to our solution, the InSAR-derived coseismic fault plane should correspond to a segment of the Eastern Maidan Fault. However, it should be noted that, apart from the northeast and southwest terminations of the geodetic-derived fault models, the position of the central part of our fault plane slightly deviates from the mapped surface trace

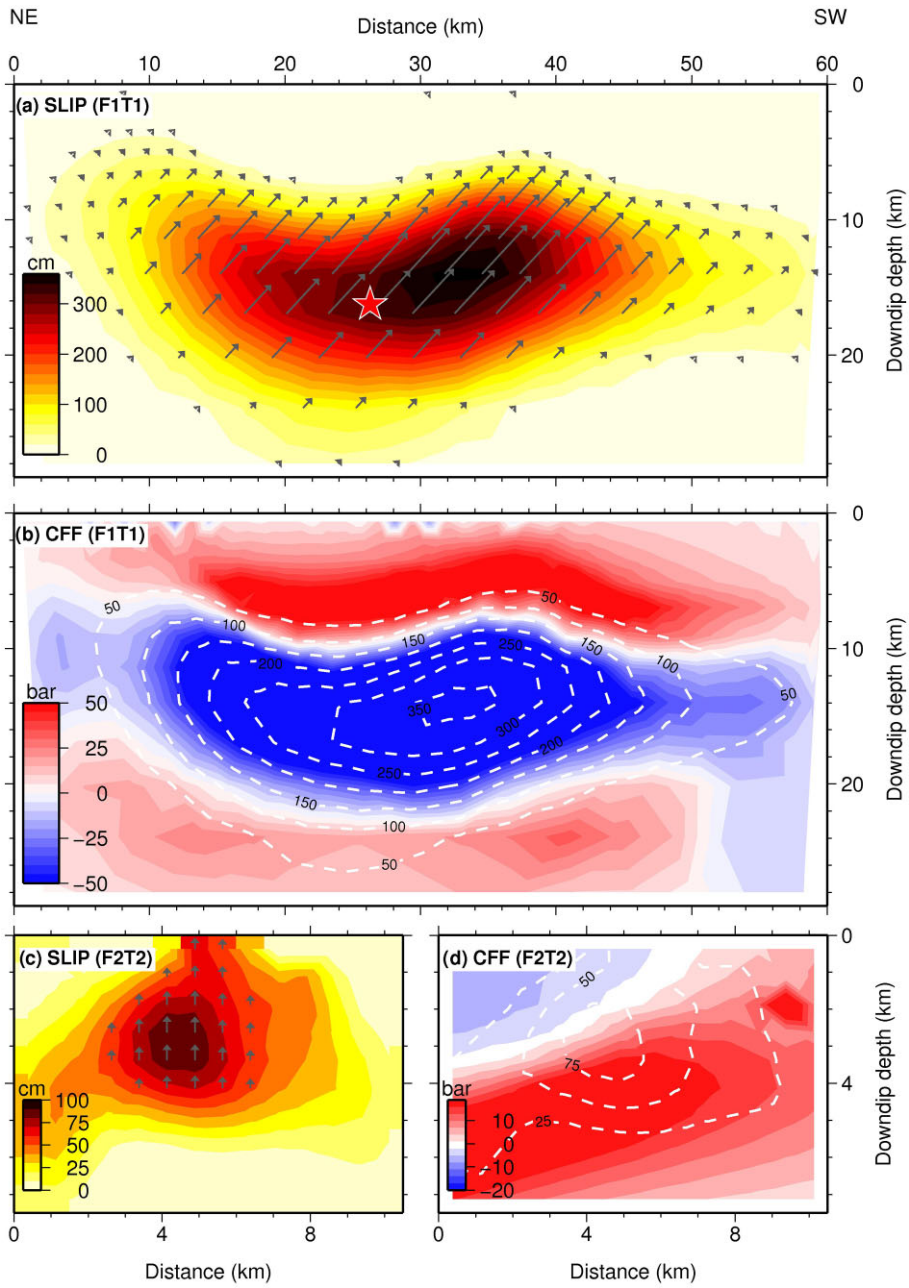

Figure 7. Slip distribution on the modelled fault planes and Coulomb stress changes. (a) Coseismic slip distribution (T1). (b) Changes in Coulomb stress on the main fault plane induced by the January 22 mainshock, assuming an effective friction of 0.4 as commonly used in stress interaction studies (e.g. Freed *et al.* 2005; Akinci & Antonioli 2013). (c) Slip distribution of the January 29 aftershock (T2). (d) Changes in Coulomb stress on the secondary SE-dipping plane induced by the mainshock. Contour lines (in cm) indicate mainshock (in panels a and b) and aftershock (in panel c) slip distribution, respectively. The star marks mainshock hypocentre (USGS 2024). Arrows in panels (a) and (c) indicate slip direction.

of the Maidan Fault (Wu *et al.* 2024; Fig. 5), being located about 10 km southwards. As this could be due to the simplified planar geometry assumed for the dislocation model, we further investigated this issue by fixing the top of our model in correspondence of the surface trace of the Maidan Fault and inverting the data again. The results show that fixing the top of the fault in this way (Fig. S10, Supporting Information), regardless of the dip angle, the InSAR data cannot be adequately reproduced (the RMS increases significantly; Table S3 model-A and Fig. S11, Supporting Information), as the fault plane is located too far north relative to the observed deformation field.

Prior to the 2024 seismic sequence, the Maidan Fault had not experienced historical ruptures, but paleoseismological evidence suggested the presence of a potential seismic gap (Wu *et al.* 2020). This finding supports the hypothesis that significant shortening still pervades the Tian Shan orogeny. Although an in-depth analysis and modelling of the interseismic deformation of the area is not the subject of our work, by comparing topography, coseismic deformation and GNSS velocities projected along a profile roughly perpendicular to the Maidan Fault (Fig. S12, Supporting Information), it is possible to observe that the interseismic GNSS velocities show a marked reduction of approximately 4 mm yr^{-1} across the Maidan

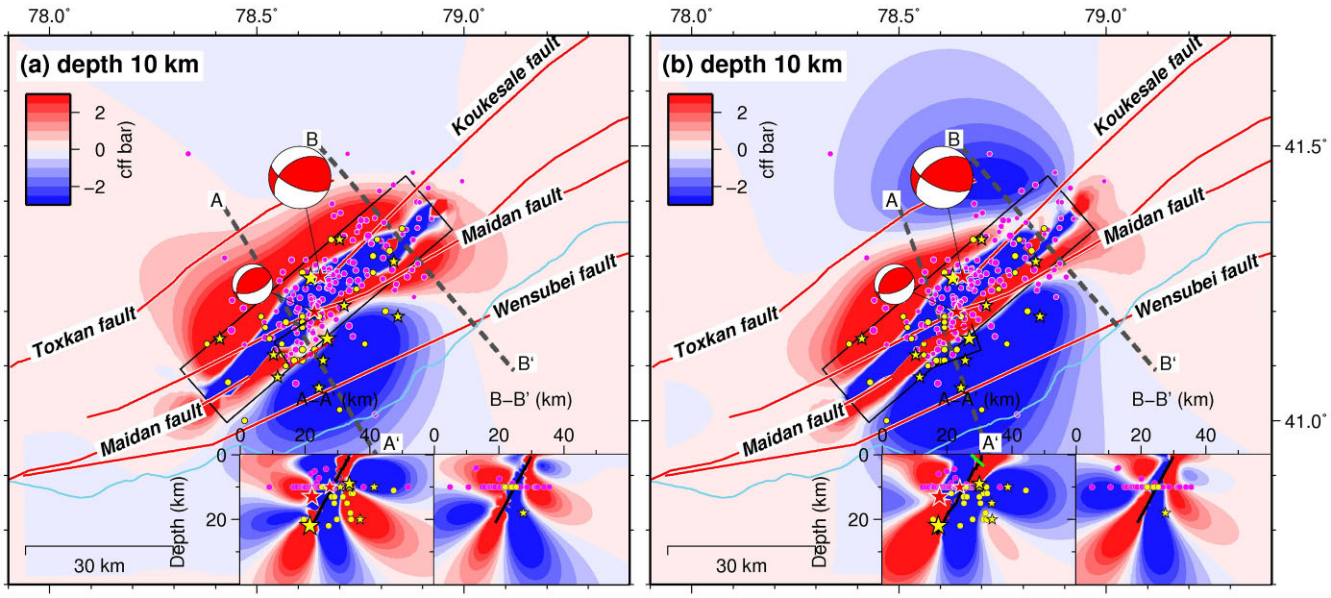

Figure 8. Coulomb stress changes produced by the 2024 January 22 M_W 7.0, Wushi earthquake. The Coulomb stress changes are computed at a depth of 10 km. Coulomb stress profiles: perpendicular to the modelled fault, showing stress imparted by our preferred solution on (a) NW-dipping thrust faults, and on (b) SE-dipping thrust faults together with aftershocks. Seismicity: magenta circles are aftershocks from USGS catalogue (USGS 2024); yellow circles are $M > 4$ events from Liang *et al.* (2024); the stars are the largest events of the seismic sequence (the red ones are from USGS, while the yellow one is from Liang *et al.* (2024)). The beach-balls display the mainshock and greatest aftershock focal solutions from the USGS catalogue (USGS 2024). The grey line in sections A-A′ and B-B′ represent our best-fit coseismic model, while the green line in section A-A′ of panel (b) is SE-dipping secondary fault modelled in the post-seismic deformation. Other symbols as in Fig. 5. Note that many hypocentres were located at a fixed depth of 10 km from the USGS location.

fault, in agreement with the recent work of Guo *et al.* (2024). In this context, our preferred fault plane and coseismic slip distribution would be located approximately at the top of the interseismic dislocation model imaged by the modelling of the interseismic GNSS data (Guo *et al.* 2024), confirming that the 2024 earthquake occurred in correspondence of the highest strain-rate sector of the transect. The comparison between the surface expression of our fault model and the topography (Fig. 9 and Fig. S12, Supporting Information) reveals that most of the activity along the Maidan Fault is concentrated near the relief margin, where the Tarim Basin intersects with the foothills of the southern Tian Shan Mountains. Observing the topographic profiles (Fig. 9), one can note how a step is present along the maximum and minimum profiles (especially along sections C–C′, D–D′, E–E′), likely representing the long-term activity of the Maidan Fault. In the case of the 2024 earthquake, the rupture was blind, as clearly shown by the continuity of the InSAR fringes and the slip distribution in the geodetic model. However, it is obvious that repeated linear morphogenic earthquakes (*sensu* Caputo 2005) have occurred along this major tectonic structure to progressively and cumulatively create this marked topographic step. This finding confirms that high-angle transpressive faults accommodate some shortening at the intersection between the relief margin and the adjacent basin in the western Tian Shan.

The calculated seismic moment release for the mainshock of 3.80×10^{19} Nm, equivalent to a moment magnitude (M_W) of 7.02, aligns well with magnitude estimates independently provided by different institutions, such as the USGS in 2024 and previous studies (Guo *et al.* 2024; Nai *et al.* 2025; Yu *et al.* 2024). This agreement emphasizes the reliability and robustness of the geodetic inversion methodology also in estimating seismic moment release. The geodetic inversion results provide valuable insights into the slip distribution characteristics of the mainshock documenting that most of the coseismic slip was concentrated on a prominent ENE–WSW oriented asperity, where slip reached a peak of approximately 3.5 m, suggesting a bilateral directivity of the Wushi mainshock rupture propagation. This concentrated slip pattern suggests a focal area of intense strain release within the fault system. Interestingly, the slip distribution analysis indicates that most of the slip appears to have occurred in horizontally elongated patches, primarily confined below depths of 10 km, in agreement with previous geodetic studies (Guo *et al.* 2024; Nai *et al.* 2025; Yu *et al.* 2024). As a matter of fact, the slip during the January 22 earthquake did not reach the surface, however there is paleoseismological evidence of large surface-rupturing events (Wu *et al.* 2020) during the Late Quaternary period, with the Maidan Fault indeed associated to linear morphogenic earthquakes (Caputo 2005) also during the Holocene. We suggest, therefore, that the Maidan fault could release accumulated tectonic strain through a wide range of magnitudes.

The observed slip arrest in the shallower sections of the fault may be attributed to various factors. Studies on reverse faulting earthquakes have in fact indicated the potential influence of lithological and/or structural controls, such as up-dip slip segmentation, on the depth extent of rupture propagation in intracontinental settings (e.g. Elliott *et al.* 2011, 2015; Copley *et al.* 2015; Mackenzie *et al.* 2016). In this regard, up-dip slip segmentation may introduce complexities in the rupture process, potentially delaying rupture propagation between different segments of the fault, as observed globally in recent years (e.g. Elliott *et al.* 2011). Therefore, as already suggested by previous studies (Guo *et al.* 2024), it is possible that part of the stress released during the 2024 sequence was absorbed by folding of the sedimentary units or by means of aftershocks and/or afterslip on unruptured portions of the coseismic fault plane. Considering these areas have been dynamically loaded resulting in a positive Coulomb stress change (Fig. 7b), new asperities and/or secondary faults, either synthetic and antithetic ones, could potentially serve as sites for future ruptures. This observation could have an important

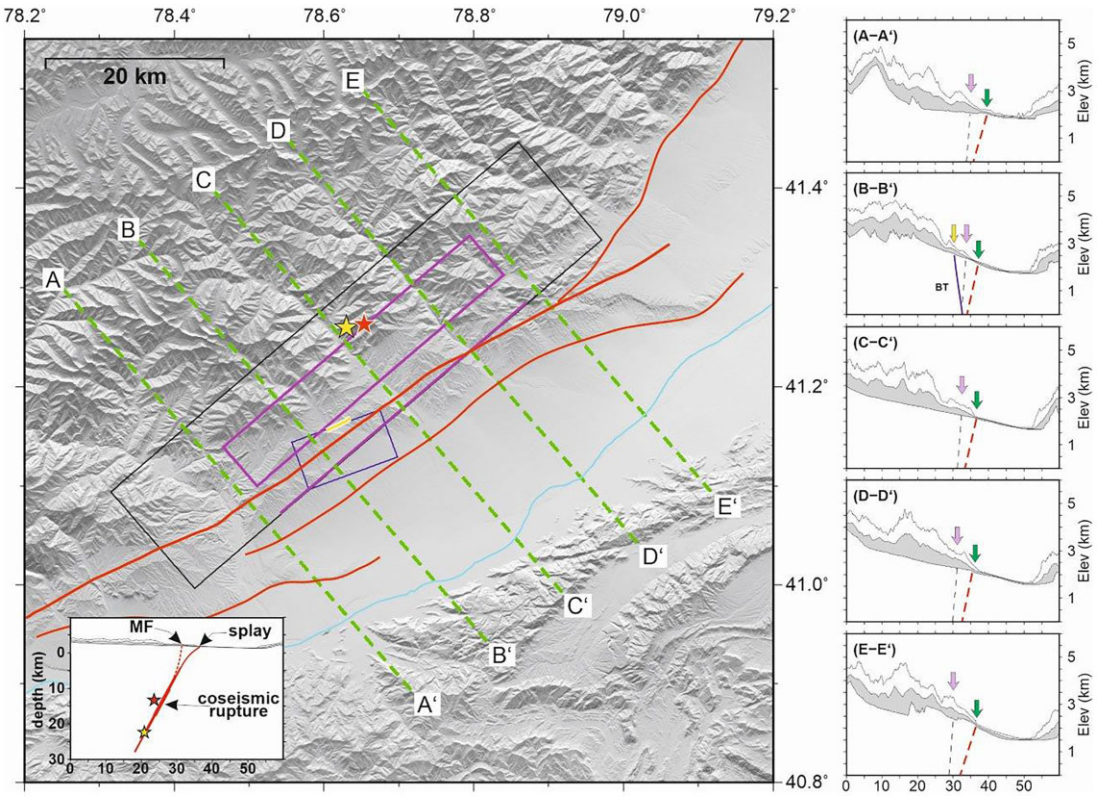

Figure 9. Topography, active structures and topographic swath profiles. In the main figure, the violet box represents our best-fit uniform slip model, while the blue box is the aftershock source. The yellow dashed line shows observed surface ruptures. Solid red lines denote major morphotectonic lineaments characterizing the area (modified from Wu *et al.* 2024). The right panels show topographic data (from the 30 m shuttle radar topography mission (SRTM) DEM) (maximum, minimum and average altitudes) projected onto the N139° direction from 10 km wide swaths. The grey dashed line indicates the up-dip projection of the geodetic fault that ruptured during the 2024 Wushi earthquake, while the red one is the geological splay. The blue line represents the back-thrust (BT). Violet and green arrows show the geodetic-inferred main fault and splay trace intersection along the profiles, while the yellow arrow indicates surface ruptures. The inset shows the relationship between the 2024 coseismic rupture fault, the geological splay and topography. MF: Maidan Fault. Other symbols as in Fig. 1.

impact on the seismic hazard assessment of the region, highlighting the importance of considering both shallow and deep segments of seismogenic faults in seismic risk mitigation strategies.

As regards the source of the post-seismic deformation, that includes the January 29 M_W 5.7 event, we performed several inversions varying the geometry and position of the structure responsible for the post-seismic deformation to discriminate between possible candidates. The dislocation modelling of InSAR data has revealed that the observed deformation was caused by the rupture of a shallow ∼40° SE-dipping, ∼10 km-long back-thrust (rake ∼90°), with a maximum slip of about 90 cm, and the rupture reaching the surface in correspondence with the observed surface breaks (Zhang *et al.* 2024), confirming that the M_W 5.7 aftershock occurred on a distinct source with respect to the mainshock one. The calculated seismic moment released in this case (0.07×10^{19} Nm, equivalent to an M_W of 5.85) aligns well with magnitude estimates (M_W 5.7–5.8) provided by different studies for the January 29 aftershock (Liang *et al.* 2024; USGS 2024).

We also calculated the static Coulomb stress changes from our preferred coseismic model to investigate the potential triggering relationship between mainshock and aftershock deformation, as well as the state of stress on other faults in the southwestern Tian Shan region. Coulomb stress changes suggest that the M_W 5.7 aftershock on the back-thrust was likely triggered by the preceding January 22 mainshock, with the reactivated slip plane correlating well with a volume of maximum stress change. The same analysis also indicates an increase of the Coulomb stress at both terminations of the major rupture surface at hypocentral depth, as well as on the parallel Toxkan fault located northwards of the Maidan fault.

In conclusion, the analysis of the 2024 Wushi seismic sequence underscores the critical role of dense, high-quality geodetic surface displacements in accurately estimating the location and the coseismic behaviour of seismogenic faults. The exceptional quality of the coseismic interferograms (Fig. 2), notable for their coherence and the clarity of the interferometric fringes, has allowed for a well-constrained determination of the coseismic model parameters (Table 1). Within this framework, our modelling reveals robust features, including the position and depth of the upper edge of the mainshock fault, as well as the absence of significant shallower slip during the investigated earthquake. Taking into account paleoseismological and morphotectonic evidence clearly documenting the frequent occurrence of linear morphogenic earthquakes (i.e. rupturing up to the topographic surface), our results suggest that the interseismic deformation accumulated on the fault was not entirely released during the Wushi earthquake. Moreover, we had the possibility to observe the occurrence of notable deformation on a shallow back-thrust that underwent significant surface rupture in contrast with the main coseismic rupture that was blind. These observations should be carefully taken into account when trying to correlate surface faulting evidence with the main coseismic rupture plane at depth because the latter could be blind and the former

could occur on secondary relatively shallow tectonic structures. In any case, extensive documentation of Late Quaternary surface ruptures along the Maidan Fault (Wu *et al.* 2020), combined with GNSS studies indicating that the fault is currently locked without evidence of significant creep deformation (Li *et al.* 2022), suggests that the upper portion of this fault still poses a considerable seismic hazard. In conclusion, our findings indicate that further aseismic deformation and/or significant earthquakes in both the shallow and deeper sectors of the Maidan fault cannot be ruled out in the future and this should be considered for a better mitigation policy of the seismic hazard affecting the Wushi County and its surrounding areas.

ACKNOWLEDGMENTS

We would like to thank the Editors Dr Eiichi Fukuyama and Prof. Bert Vermeersen, and three anonymous reviewers for their constructive suggestions, which helped to improve the manuscript. All the figures were made using the GMT software (Wessel & Smith 1998). Sentinel-1 data are copyright of Copernicus (2024).

SUPPORTING INFORMATION

Supplementary data are available at *GJIRAS* online.

Please note: Oxford University Press is not responsible for the content or functionality of any supporting materials supplied by the authors. Any queries (other than missing material) should be directed to the corresponding author for the paper.

DATA AVAILABILITY

Seismicity used for this research is found online (USGS catalogue, available at https://earthquake.usgs.gov/earthquakes/map/). The down-sampled InSAR (Sentinel-1) data used for geodetic modelling in this study, as well as the slip models and the Coulomb stress change distributions shown in Figs 5–8 are available in the zenodo data repository https://doi.org/10.5281/zenodo.14795056.

REFERENCES

Akinci, A. & Antonioli, A., 2013. Observations and stochastic modelling of strong ground motions for the 2011 October 23 Mw 7.1 Van, Turkey, earthquake, *Geophys. J. Int.,* **104,** 1400.

Atzori, S. *et al.*, 2009. Finite fault inversion of DInSAR coseismic displacement of the 2009 L'Aquila earthquake (Central Italy), *Geophys. Res. Lett.,* **36**(15), L15305, doi:10.1029/2009GL039293.

Avouac, J.P., Tapponnier, P., Bai, M.X., You, H.C. & Wang, G., 1993. Active faulting and folding in the northern Tian Shan and rotation of Tarim relative to Dzungarian and Kazakhstan, *J. geophys. Res.,* **98**(B4), 6755–6804.

Caputo, R., 2005. Ground effects of large morphogenic earthquakes, *J. Geodyn.,* **40**(2-3), 113–118.

Cheloni, D. *et al.*, 2010. Coseismic and initial post-seismic slip of the 2009 Mw 6.3 L'Aquila earthquake, Italy, from GPS measurements, *Geophys. J. Int.,* **181,** 1539–1546.

Cheloni, D. *et al.* 2016. New insights into fault activation and stress transfer between en echelon thrusts: the 2012 Emilia, Northern Italy, earthquake sequence, *J. geophys. Res.* **121**(6), 4742–4766.

Cheloni, D., Famiglietti, N.A., Caputo, R., Tolomei, C. & Vicari, A., 2024, A composite fault model for the 2024 Mw 7.4 Hualien earthquake sequence in Eastern Taiwan inferred from GNSS and InSAR data, *Geophys. Res. Lett.,* **51**(2), doi: 10.1029/2024GL110255.

Copley, A., Karasozen, B., Elliott, J.R., Samsonov, S. & Nissen, K., 2015. Seismogenic faulting of the sedimentary sequence and laterally-variable material properties in the Zagros Mountain (Iran) revealed by the August 2014 Murmuri (Dehloran) earthquake sequence, *Geophys. J. Int.,* **203,** 1436, doi:10.1093/gji/ggv365.

Corana, A., Marchesi, M., Martini, C. & Ridella, S., 1987. Minimizing multimodal functions of continuous variables with the "Simulated Annealing" algorithm, *ACM Trans. Math. Softw.,* **13**(3), 262–280.

Costantini, M., 1998. "A novel phase unwrapping method based on network programming", *IEEE Trans. Geosci. Remote Sens.,* **36**(3), 813–821.

Elliott, J.R. *et al.* 2015. The 2013 Mw 6.2 Khaki-Shonbe (Iran) Earthquake: insights into seismic and aseismic shortening of the Zagros sedimentary cover, *Earth Space Sci*., **2**(11), 435–471

Elliott, J.R., Parsons, B., Jackson, J.A., Shan, X., Sloan, R.A. & Walker, R.T., 2011. Depth segmentation of the seismogenic continental crust: the 2008 and 2009 Qaidam earthquakes, *Geophys. Res. Lett.,* **38**(6), n/a–n/a, doi:10.1029/2011GL046897.

Famiglietti, N.A. *et al.*, 2022. The 2021 Greece Central Crete M_L 5.8 earthquake: an example of coalescent fault segments reconstructed from InSAR and GNSS data, *Remote. Sens.,* **14**(22), 5783, doi:10.3390/rs14225783.

Freed, T.G., 2005. Earthquake triggering by static, dynamic, and postseismic stress transfer, *Annu. Rev. Earth Planet. Sci.,* **33,** 335, doi:10.1146/annurev.earth.33.092203.122505.

Ghulam, A., Amer, R. & Ripperdan, R., 2010. A filtering approach to improve deformation accuracy using large baseline, low coherence DInSAR phase images, *Paper presented at IGARSS 2010 Symposium*. IEEE International Geoscience and Remote Sensing Symposium.

Goldstein, R.M. & Werner, C.L., 1998. Radar interferogram filtering for geophysical applications, *Geophys. Res. Lett.,* **25** *(* 21 *),* 4035–4038.

Golshadi, Z., Famiglietti, N.A., Caputo, R., SoltaniMoghadam, S., Karimzadeh, S., Memmolo, A., Falco, L. & Vicari, A., 2023. Contemporaneous thick- and thin-skinned seismotectonics in the external zagros: the case of the 2021 fin doublet, Iran, *Remote. Sens.,* **15**(12), 2981, doi:10.3390/rs15122981.

Guo, N., Wu, Y., Zhu, S. & Chen, C., 2024. Coseismic deformation and interseismic strain accumulation of the 2024 Ms 7.1 Wushi earthquake in Xinjiang, China, *Adv. Space Res.,* **74,** 1586–1594.

Huang, W., Yang, X., Li, A., Pierce, I., Thompson, J., Angster, S. & Zhang, L., 2015. Late pleistocene shortening rate on the northern margin of the Yanqi Basin, southeastern Tian Shan, NW China, *J. Asian Earth Sci.,* **112,** 11–24.

Krüger, F., Kulikova, G. & Landgraf, A., 2015. Instrumental magnitude constraints for the 11 July 1889, Chilik earthquake, *Geol. Soc. Lond. Sp. Publ.,* **432,** 432, doi:10.1144/SP432.8.

Kulikova, G. & Krüger, F., 2015. Source process of the 1911 M8.0 Chon-Kemin earthquake: investigation results by analogue records, *Geophys. J. Int.,* **201**(3), 1891–1911.

Kulikova, G. & Krüger, F., 2017. Historical seismogram reproductions for the source parameters determination of the 1902, Atushi (Kashgar) earthquake, *J. Seismol.,* **21**(6), 1577–1597.

Li, A., Ran, Y.K., Xu, L.X., Liu, G.H. & Li, Y.B., 2013. Paleoseismic study of the east Kalpintage fault in southwest Tianshan based on deformation of alluvial fans and ^{10}Be dating, *Nat. Hazards,* **68**(92), 1075–1087.

Li, J., Yao, Y., Li, R., Yusan, S., Li, G., Freymneller, J.T. & Wang, Q., 2022. Present-day strike-slip faulting and thrusting of the Kepintage Fold-and-Thrust Belt in Southern Tianshan: constraints from GPS observations, *Geophys. Res. Lett.,* **49,** 1–11.

Li, Y., Liu, M., Hao, M., Zhu, L., Cui, D. & Wang, Q., 2021. Active crustal deformation in the Tian Shan region, central Asia, *Tectonophysics,* **811,** 228 868, doi:10.1016/j.tecto.2021.228868.

Liang, S.S., Zou, L.Y., Liu, Y.Q., Li, X. & Ren, X., 2024. Determination of focal mechanism solutions of the earthquakes with M > 4.0 occurred in the mainland of China during November 2023 to February 2024, *Prog. Earthq. Sci.* **54**(3), doi:10.19987/j.dzkxjz.2024-036.

Lin, J. & Stein, R.S., 2004. Stress triggering in thrust and subduction earthquakes, and stress interaction between the southern San Andreas and nearby thrust and strike-slip faults, *J. geophys. Res.,* **109,** B02303, doi:10.1029/2003JB002607.

Lin, J., Stein, R.S., Meghraoui, M., Toda, S., Ayadi, A., Dorbath, C. & Belabbes, S., 2011. Stress transfer among en echelon and opposing thrusts and tear faults: triggering caused by the 2003 Mw = 6.9 Zemmouri, Algeria, earthquake, *J. geophys. Res.,* **116**(B03305), doi:10.1029/2010JB007654.

Lohman, R.B. & Simons, M., 2005. Some thoughts on the use of InSAR data to constrain models of surface deformation: noise structure and data downsampling, *Geochem. Geophys. Geosyst.,* **6**(Q01007), doi:10.1029/2004GC000841.

Mackenzie, D., Elliott, J.R., Altunel, E., Walker, R.T., Kurban, Y.C., Schwenninger, J.-L. & Parsons, B., 2016. Seismotectonics and rupture process of the Mw 7.1 2011 Van reverse-faulting earthquake, Eastern Turkey, and implications for hazard in regions of distributed shortening, *Geophys. J. Int.,* **206**(1), 501–524.

Molnar, P. & Ghose, S., 2000, Seismic moment of major earthquakes and the rate of shortening across the Tien Shan, *Geophys. Res. Lett.,* **27**(16), 2377–2380.

Nai, Y., Han, B., Liu, Z., Li, Z., Song, C., Yu, C., Li, S. & Peng, J., 2025. Coseismic surface displacements and source model of the 2024 Mw 7.0 Wushi (Xinjiang, China) earthquake revealed by InSAR observations, *Geomatics and Information Science of Wuhan University*.**50,** doi:10.13203/j.whugis20240037.

Okada, Y., 1985. Surface deformation due to shear and tensile faults in a half-space, *Bull. seism. Soc. Am.,* **75** *(* 4*),* 1135–1154.

Press, W.H., Teukolsky, S.A., Vetterling, W.T. & Flannery, B.P., 1992, *Numerical Recipes in C: the Art of Scientific Computing,* 2nd edn., Cambridge University Press, pp. 262–280.

Qiu, J., Ji, L., Zhu, L. & Wang, Q., 2022. Present-day tectonic deformation partitioning across South Tianshan from satellite geodetic imaging, *Front. Earth Sci.,* **9,** 793 890, doi:10.3389/feart.2021.793890.

Reigber, A. & Moreira, J& IEEE Publications., 1997, Phase unwrapping by fusion of local and global methods, *Proceedings of IGARSS'97 Symposium*.

Shen, Z.-K., Wang, M., Li, Y.X., Jackson, D.D., Yin, A., Dong, D.A. & Fang, P., 2001. Crustal deformation along the Altyn-Tagh fault system, western China, from GPS, *J. geophys. Res.,* **106**(B12), 30 607–30 621,

Stark, P.B. & Parker, R.L., 1995. Bounded-values least-squares algorithm—an algorithm and implications, *Comput. Stat.,* **10** *(* 2*),* 129–141.

Takaku, J., Tadono, T. & Tsutsui, K., 2014. Generation of high resolution global DSM from ALOS PRISM., the international archives of the photogrammetry, In *Remote Sensing and Spatial Information Sciences*Vol. **XL-4,** pp. 243–248, ISPRS.

Thompson, S.C., Weldon, R.J., Rubin, C.M., Abdrakhmatov, K., Molnar, P. & Berger, G.W., 2002. Late quaternary slip rates across the central Tien Shan, Kyrgyzstan, central Asia, *J. geophys. Res.,* **107**(B9), doi:10.1029/2001JB000596.

U.S. Geological Survey, 2024. Earthquake Hazards Program, available at:http://earthquake.usgs.gov/earthquakes/map; last accessed on 6 March 2024.

Wang, M. & Shen, Z.-K., 2020, Present-day crustal deformation of continental China derived from GPS and its tectonic implications, *J. geophys. Res.,* **125,** 125.

Wessel, P. & Smith, W.H.F., 1998. New improved version of the generic mapping tools released, *EOS Trans. Am. geophys. Un.,* **79** *(* 47*),* 579–579.

Wu, C. *et al.* 2019. Oblique thrust of the Maidan fault and late quaternary tectonic deformation in the southwestern Tian Shan, northwestern China, *Tectonics,* **38,** 2625–2645.

Wu, C., Zheng, W., Zhang, Z., Jia, Q. & Yang, H., 2020, Large-earthquake rupturing and slipping behavior along the range-front Maidan fault in the southern Tian Shan, northwestern China, *J. Asian Earth Sci.,* **190,** doi:10.1016/j.jseaes.2019.1041.93.

Wu, X. *et al.*, 2024. The China active faults database and its web system, *Earth Syst. Sci. Data,* **16,** 3391–3417.

Yin, A., 2010, Cenozoic tectonic evolution of Asia: a preliminary synthesis, *Tectonophysics,* **488,** 293–325.

Yu, S., Li, Z., Zhao, P., Luo, J. & Yang, Y., 2024. Source Parameters and Seismogenic Fault Model of the 2024 Mw 7.0 Wushi (Xinjiang, China) Earthquake Revealed by InSAR Observations, *Pure and Applied Geophysics,*doi: 10.1007/s00024-024-03531-y.

Yushan, A., Yusan, S., Liu, D., Li, J., Yasen, A., Liu, J. & Chen, L., 2022. Double rupture event in the Tianshan Mountains: a case study of the 2021 Mw 5.3 Baicheng earthquake, NW China, *Open Geosci.,* **14,** 1667–1677.

Zhang, B.-X., Qian, L., Li, T. *et al.*, 2024, Geological disasters and surface ruptures of January 23, 2024 Ms 7.1 Wushi earthquake, Xinjiang, China, *Seismol. Geol.,* **46**(1), doi:10.3969/j.issn.0253-4967.2024.01.013.

Zubovich, A.V. *et al.*, 2010. GPS velocity field for the Tien Shan and surrounding regions, *Tectonics,* **29,** n/a, doi:10.1029/2010TC002772.